Published as: *Structure*. 2010 September 08; 18(9): 1159–1170.

Crystal Structures of RMI1 and RMI2, Two OB-fold Regulatory Subunits of the BLM Complex

Feng Wang[1,2], **Yuting Yang**[1,2], **Thiyam Ramsing Singh**[3], **Valeria Busygina**[4], **Rong Guo**[5], **Ke Wan**[1,2], **Weidong Wang**[5], **Patrick Sung**[4], **Amom Ruhikanta Meetei**[3], and **Ming Lei**[1,2]

[1]Howard Hughes Medical Institute, University of Michigan Medical School, 1150 W. Medical Center Drive, Ann Arbor, MI 48109

[2]Department of Biological Chemistry, University of Michigan Medical School, 1150 W. Medical Center Drive, Ann Arbor, MI 48109

[3]Division of Experimental Hematology and Cancer Biology, Cincinnati Children's Research Foundation and University of Cincinnati College of Medicine, Cincinnati, OH 45229

[4]Department of Molecular Biophysics and Biochemistry, Yale University School of Medicine, New Haven, CT 06520

[5]Laboratory of Genetics, National Institute of Aging, National Institutes of Health, Baltimore, MD 21224

Summary

Mutations in BLM, a RecQ-like helicase, are linked to the autosomal recessive cancer-prone disorder Bloom's syndrome. BLM associates with Topoisomerase(Topo) IIIα, RMI1 and RMI2 to form the BLM complex that is essential for genome stability. The RMI1-RMI2 heterodimer stimulates the dissolution of double Holliday junction into non-crossover recombinants mediated by BLM-Topo IIIα and is essential for stabilizing the BLM complex. However, the molecular basis of these functions of RMI1 and RMI2 remains unclear. Here we report the crystal structures of multiple domains of RMI1-RMI2, providing direct confirmation of the existence of three oligonucleotide/oligosaccharide binding (OB)-folds in RMI1-RMI2. Our structural and biochemical analyses revealed an unexpected insertion motif in RMI1N-OB, which is important for stimulating the dHJ dissolution. We also revealed the structural basis of the interaction between RMI1C-OB and RMI2-OB and demonstrated the functional importance of the RMI1-RMI2 interaction in genome stability maintenance.

*Correspondence: leim@umich.edu (M.L.).

Accession number: The coordinates and structure factors of RMI1N and the RMI1C-RMI2 complex have been deposited in the RCSB Protein Data Bank under accession code 3NBI and 3NBH, respectively.

Introduction

Bloom syndrome (BS) is a rare autosomal recessive disorder characterized by growth retardation, sunlight sensitivity, and a predisposition to the development of various types of cancer in early life (Bachrati and Hickson, 2008). Cells from BS patients display elevated level of chromosomal instability, manifested by high frequency of sister chromatid exchanges (SCEs). SCEs arise from crossing over of chromatid arms during homologous recombination (HR). Whereas crossing over is required in meiosis, it can in mitotic cells be associated with a detrimental loss of heterozygosity, a common feature in neoplastic cells. The gene mutated in BS, *BLM*, encodes one of the five RecQ helicase family members in human (Ellis et al., 1995). The RecQ family helicases play important roles in genome stability maintenance. Mutations in two other human RecQ helicases, WRN and RECQ4, are the causes of Werner's syndrome and Rothmund-Thomson syndrome, respectively. Both diseases are linked with premature aging, genomic instability, and predisposition to a spectrum of cancers (Bachrati and Hickson, 2008).

BLM binds directly to a type IA topoisomerase, topoisomerase (Topo) IIIα, to dissolve double Holliday junction (dHJ) intermediates into non-crossover recombinants (Plank et al., 2006; Wu and Hickson, 2003). This dissolution activity of the BLM-Topo IIIα complex is thought to be critical for suppressing DNA crossover formation in mitotic cells and cancer avoidance in humans. The complex might also process many other DNA structures, such as stalled replication forks (Ralf et al., 2006) and has been implicated in checkpoint signaling and responses during DNA damage (Beamish et al., 2002; Davies et al., 2004). The BLM-Topo IIIα interaction is conserved in evolution; for example, the *Saccaromyces cerevisiae* ortholog of BLM, Sgs1, also forms a complex with yeast topoisomeriase III (Top3) (Bennett et al., 2000; Gangloff et al., 1994).

The dHJ dissolution activity of the BLM-Topo IIIα complex requires a third component, RMI1 (*R*ecQ *m*ediated genome *i*nstability 1 or BLAP75) (Chen and Brill, 2007; Raynard et al., 2006). RMI1 is an evolutionarily conserved integral component of the BLM-Topo IIIα complex as the yeast ortholog Rmi1 was also identified as a subunit of the Sgs1-Top3 complex (Chang et al., 2005; Mullen et al., 2005). RMI1 strongly stimulates the dHJ dissolution activity of BLM-Topo IIIα *in vitro* (Bussen et al., 2007; Raynard et al., 2006; Raynard et al., 2008), which is crucial in suppressing aberrant chromosomal rearrangement as loss of RMI1 led to discruption of the BLM-Topo IIIα complex and an increased level of SCEs (Yin et al., 2005).

Recently, RMI2 (or BLAP18) was identified, which is essential for the BLM-Topo IIIα complex (Singh et al., 2008; Xu et al., 2008a). Depletion of RMI2 resulted in complex destabilization and increased SCEs. The association of RMI2 with the BLM-Topo IIIα complex is though RMI1 (Xu et al., 2008a). Primary sequence analysis indicated that both RMI1 and RMI2 are oligonucleotide/oligosaccharide binding (OB)-fold-containing proteins. RMI1 has two putative OB-folds at both termini while RMI2 only contains one. Moreover, the alignment also showed a potential structural similarity between RMI1-RMI2 and the RPA70-RPA32 complex (Singh et al., 2008; Xu et al., 2008a). RPA70 and RPA32 are subunits of the eukaryotic, non-specific single-stranded (ss) DNA-binding protein complex

replication protein A (RPA), which mediates critical and diverse DNA transactions throughout the genome. RPA in total contains six OB-folds: RPA70 contains four, whereas RPA32 and RPA14 have one each (Bochkarev and Bochkareva, 2004; Bochkarev et al., 1999; Kerr et al., 2003). While RMI2 is most similar to the OB-fold in RPA32, the C-terminal RMI2-binding domain of RMI1 (RMI1C) exhibits limited sequence similarity to the C-terminal OB-fold of RPA70 (RPA70C). However, sequence comparison failed to disclose any convincing similarity between the N-terminal domain of RMI1 (RMI1N) and any OB-fold in the RPA complex (Xu et al., 2008a). Because OB-folds are well known for the absence of reliable primary sequence features that can be used for accurate prediction, decisive confirmation of the existence of OB-folds in RMI1 and RMI2 and the similarity between RMI1-RMI2 and RPA70-RPA32 requires structural characterization of the RMI1-RMI2 complex.

In this report, we provide structural and functional analyses of RMI1 and RMI2. The crystal structures of RMI1N and the RMI1C-RMI2 complex confimed the existence of three OB-folds in RMI1-RMI2. Our data revealed an unexpected insertion motif in the OB-fold of RMI1N, which is essential for the BLM-Topo IIIα-mediated dHJ dissolution. We also uncovered the structural basis of the interaction between the two OB-folds in RMI1C and RMI2 and demonstrated the functional importance of the RMI1C-RMI2 interaction in the genome stability maintenance.

Results

Structural determination of the conserved N-terminal domain of RMI1

In order to gain insight into the structural domains in RMI1, we performed a secondary structural analysis using the program PredictProtein (Rost et al., 2004), which accurately predicted the positions of most of the α helices and β strands in several proteins in our previous studies (Sun et al., 2009; Zeng et al.). This analysis predicted that RMI1 consists of two structural domains (Figure 1A). RMI1N contains two motifs, DUF1767, a conserved region with unknown function, and a putative OB-fold (Briggs et al., 2005; Xu et al., 2008a). RMI1C bears only one putative OB-fold that is similar to RPA70C (Xu et al., 2008a). Between the N- and the C-terminal domains there is a large fragment (~270 resides) that exhibits no detectable feature of secondary structure. Notably, among these three regions of RMI1, RMI1N is the only region of RMI1 that is conserved across all species from vertebrates to yeast (Figure 1C). Consistent with this high degree of conservation, RMI1N is required for the associations of both BLM and Topo IIIα with RMI1 (Raynard et al., 2008) and plays an essential role in BLM-Topo IIIα-mediated dHJ dissolution (Bussen et al., 2007; Raynard et al., 2008). The extensive sequence homology and important functions of RMI1N prompted a rigorous structural. The crystal structure of human RMI1N was determined by single-wavelength anomalous dispersion (SAD) using Se-Met substituted crystals at 2.0 Å resolution (Figure 1B, S1A) (Table S1).

The crystal structure of RMI1N

The structure reveals that the core of RMI1N is indeed made up of one single OB-fold as expected from previous sequence analysis (Figure 1B) (Xu et al., 2008a). N-terminal to the

OB-fold is a three-helix bundle, corresponding to the conserved DUF1767 motif (Figures 1A and B). This helical region protrudes to one side of the structure and makes extensive hydrophobic contacts with the convex side of the β-barrel (Figure 1B). Strikingly, RMI1N contains a large insertion between strands β1 and β2 (residues 96-134), part of which forms a helix (αI) that runs perpendicular to the axis of the OB-fold (Figure 1B).

Previous studies indicated a limited sequence similarity between the OB-fold in RMI1N and the "Wedge" domain in bacterial helicase RecG (Briggs et al., 2005; Xu et al., 2008a). However, a comparative structure search using the DALI server (Holm and Sander, 1991) revealed that the structure of the RMI1N OB-fold is most similar to the N-terminal OB-fold from the 70 kDa subunit of human RPA (RPA70N) (Figure 2A). The two structures can be superimposed with a root-mean-square deviation (rmsd) of 2.7 Å in the positions of 96 equivalent Cα atoms (Figure 2A). Notably, the structurally conserved region is only limited to the central β-barrel of the proteins. Neither the N-terminal three-helix-bundle motif nor the large insertion between strands β1 and β2 in RMI1N presents in RPA70N, explaining the failure to detect similarities between RMI1N and RPA70N by bioinformatic approaches.

Canonical ssDNA-binding OB-folds employ a basic groove for ssDNA association, as illustrated by the human POT1-ssDNA complex structure (Lei et al., 2004). In those structures, both basic and aromatic residues on the ssDNA-binding grooves are required for the interaction; basic residues stabilize the negative phosphate groups of the DNA backbone, whereas aromatic residues are involved in stacking with the DNA bases (Bochkarev et al., 1997; Horvath et al., 1998; Lei et al., 2003; Lei et al., 2004; Mitton-Fry et al., 2004). In contrast, although the OB-fold of RMI1N contains several basic residues, there are very few aromatic residues at the expected positions for optimal ssDNA interaction. This is consistent with our data that even at a very high protein concentration (1 mM), no RMI1N-ssDNA complex was observed in an Electrophoretic Mobility Shift Assay (data not shown). Thus, we conclude that the OB-fold in RMI1N does not possess DNA binding activity. Instead, RMI1N has been reported to mediate protein-protein interactions with both BLM and Topo IIIα and play an important role in BLM-Topo IIIα-mediated dHJ dissolution (Raynard et al., 2008). This correlates well with the fact that its closet structural homologue RPA70N is also a protein-protein interaction module (Jacobs et al., 1999; Xu et al., 2008b).

Several features of RMI1N appear to fix the relative orientation between the three-helix-bundle motif and the OB-fold core and allow RMI1N to adopt a compact globular structure resembling a single folded unit. First, the three-helix-bundle motif packs on the OB-fold core through extensive van der Waals contacts and buries an otherwise solvent exposed surface area of ~ 2,450 Å (Figure 2B). Second, the short loop between helices α1 and α2 in the three-helix bundle stabilizes the top region of the OB-fold core through two pairs of stacking interactions: His19 with Phe84, and Pro23 with His66 (Figure 2C). Consistent with these observations, our attempt to express and purify the central OB-fold core without the three-helix-bundle motif yielded only insoluble products (data not shown), suggesting that this three-helix-bundle motif is required for stablizing the OB-fold core.

A point mutation of a conserved residue in RMI1N, K166A, was reported to disrupt the RMI1-Topo IIIα interaction and abolish the stimulatory effect of RMI1 on the BLM-Topo

IIIα–mediated dHJ dissolution (Raynard et al., 2008). In the crystal structure, Lys166 from strand β4 of the OB-fold makes hydrogen-bonding interactions with three main chain carbonyl groups (Figure 2D). Thus, Lys166 functions as a molecular glue to stabilize the relative orientation between the three-helix bundle and the OB-fold core in RMI1N. The K166A mutant will disrupt this interaction network and result in a conformational change in RMI1N, which very likely will prevent the interaction between RMI1 and Topo IIIα. Further structural study of the RMI1-Topo IIIα complex is required to test this hypothesis.

The large insertion in the RMI1N OB-fold is essential for BLM-Topo IIIα-mediated dHJ dissolution

A striking feature of the RMI1N structure is the highly conserved 39-residue insertion between strands β1 and β2 (Figures 1B and C). This large insertion, containing one α-helix αI and a long partially disordered loop, adopts an extended conformation stretching away from the OB-fold of RMI1N (Figure 1B). In fact, this insertion is ordered by crystal lattice contacts with the surface of the adjacent molecule and even contacts the next but one molecule (Figure S1B). We failed to build residues between Asn110 and Glu119, and this region is presumed to be flexible within the crystal lattice.

The highly conserved nature of this insertion in RMI1 OB-fold prompted us to ask whether it will affect the RMI1-dependent stimulation of the BLM-Topo IIIα-mediated dHJ dissolution. We replaced residues 97-131 between strands β1 and β2 in RMI1N with a four-residue-linker “SGGS”, and expressed and purified the mutant protein RMI1NΔloop from *E. coli* cells (Figure S2). Gel filtration chromatographic analysis showed that RMI1NΔloop was a well-behaved protein in solution, suggesting that the large insertion was not required for the folding and/or the stability of RMI1N (Figure S2). We tested the effects of RMI1NΔloop on the BLM-Topo IIIα-mediated dHJ dissolution using a standard dHJ substrate. Dissolution of this substrate results in the release of two intact circular oligonucleotides (Wu and Hickson, 2003). As reported previously, both full-length RMI1 and RMI1N greatly enhanced the dissolution activity of BLM-Topo IIIα (Figure 3A). Strikingly, this stimulatory effect was completely abolished when RMI1NΔloop was used in the reaction (Figure 3A), suggesting that the insertion motif in the RMI1N OB-fold plays an essential role in stimulating BLM-Topo IIIα-mediated dHJ dissolution.

One explanation for the lack of stimulation on dHJ dissolution is that RMI1NΔloop loses the binding ability with BLM-Topo IIIα. To test this possibility, we expressed Flag-tagged full-length RMI1 or RMI1Δloop in HeLa cells and examined their interactions with other BLM complex components by immunoprecipitation (IP). Expression of Flag-tagged RMI1 or RMI1Δloop did not affect the stability of the endogenous BLM complex (Figure 3B). While wild-type RMI could successfully co-precipitated endogenous BLM, Topo IIIα, and RMI2, deletion of the insertion in RMI1 completely abolished the interactions between RMI1 and BLM-Topo IIIα (Figure 3B). Notably, RMI1Δloop still retained the binding ability with RMI2 (Figure 3B), consistent with previous data that RMI1C interacts with RMI2 (Singh et al., 2008; Xu et al., 2008a). Taken together, these results demonstrated that the insertion motif in RMI1N is crucial for the interaction between RMI1 and the BLM-Topo IIIα complex.

Crystal structure of the RMI1C-RMI2 complex

Sequence analysis suggested that both RMI2 and RMI1C contain OB-folds and these domains interact with each other in a manner similar to that between RPA70C and RPA32N (Xu et al., 2008a). To reveal the structural similarity between RMI1C-RMI2 and RPA70C-RPA32N, we expressed and purified the recombinant RMI1C-RMI2 complex and determined its crystal structure by SAD using Se-Met substituted crystals at 2.0 Å resolution (Table S2) (Figure S3A).

The RMI1C-RMI2 complex structure reveals a 1:1 stoichiometry between RMI1C and RMI2, correlating well the observed molecular weight of the complex as determined by gel filtration chromatography (~38 kDa, Figure S3B, C). The crystal structure shows that each protein comprises a single OB-fold (Figure 4A), consistent with previous sequence analysis (Singh et al., 2008; Xu et al., 2008a). In addition to the central β barrel, both OB-folds contain a C-terminal helix αC, which makes significant contributions to the interfaces between RMI1C and RMI2 (Figure 4A). Despite these similarities, both RMI1C and RMI2 exhibit unique structural features. Most notably, RMI1C contains a large segment (resides 558-587) in the connecting region between strands β3 and β4. This three-helix segment covers the bottom of the β-barrel and extends outside of the OB-fold core (Figure 4A). On the other hand, RMI2 has a unique insertion (residues 41–55) between αA and β1, N-terminal to the OB-fold core (Figure 4A). This insertion folds into a β hairpin (βA and βB), and together with helix αA, functions as a “lid” to cap the top of the RMI2 OB-fold.

The RMI1C-RMI2 Interaction

The interface between RMI1C and RMI2 in the crystal structure involves both hydrophobic and electrostatic interactions (Figure 4B). The intermolecular contacts are mediated primarily by the αC helices and the β-barrels of both proteins, burying ~1,285 $Å^2$ and 1,300 $Å^2$ of solvent accessible surface on RMI1C and RMI2, respectively. Notably, the αC helix of RMI2 makes a ~30° kink at residue Met134 (Figures 4B and C). As a consequence, the bended αC helix of RMI2 leans towards an extended groove formed by helix αC and one side of the RMI1C OB-fold (Figures 4B and 4C). The hydrophobic contact between the two αC helices is extensive, with four layers of interdigitating residues from both helices (Figure 4B). At the bending position of helix αC in RMI2, the side chain of Met134 is buried into a hydrophobic pocket of RMI1 (Figure 4C). Besides the contacts mediated by the αC helices, the β-barrels of both proteins also make substantial contributions to the RMI1C-RMI2 interaction. A panel of hydrophobic and aromatic residues from both RMI1 (Phe513, Val515, and Tyr540) and RMI2 (Pro21, Pro22, Trp59, and Met103) form extensive van der Waals contacts and contribute ~50% of the binding interface between RMI1C and RMI2 (Figure 4B). In addition to hydrophobic contacts, electrostatic interactions provide additional specificity and stability to the RMI1C-RMI2 complex. There are a total of eleven intermolecular electrostatic interactions, mostly located at the periphery of the RIM1-RMI2 interface. These electrostatic interactions help stabilize the bended αC helix of RMI2 on the concaved surface of RMI1C and seal the contact interface between the two β -barrels in the complex.

The structural conservation between RMI1C-RMI2 and RPA70C-RPA32N

Three-dimensional superposition revealed that the crystal structure of RMI1C-RMI2 closely resembles that of the RPA70C-RPA32N complex (Figure 5A), consistent with previous sequence alignment predictions (Singh et al., 2008; Xu et al., 2008a). The OB-folds are closely conserved, with a Cα rmsd value of 3.2 Å between the OB folds of RMI1C and RPA70C and 2.0 Å between the OB-folds of RMI2 and RPA32N (Figures 5A, B, and C). Notably, the structurally conserved region includes not only the central β-barrel of the OB-folds, but also the peripheral structural elements. First, both RMI1C and RPA70C contain a large three-helix insertion between strand β3 and β4 that caps the bottom of the OB-folds (Figures 5A and B). Second, a β hairpin (the RMI2 “lid” motif) covers the top of the (β-barrels in both RMI2 and RPA32N OB-folds (Figure 5C). In addition to similarities between the individual components, the RMI1C-RMI2 and the RPA70C-RPA32N complexes exhibit another common feature. In both cases, the two subunits heterodimerize through hydrophobic contacts mediated by the two C-terminal αC helices (Figure 5A). Taken together, we conclude that RMI1C-RMI2 is structurally similar to the RPA70C-RPA32N complex. In the RPA complex, the C-terminal helices from all three components (RPA70, RPA32, and RPA14) protrude away from the OB-fold cores to interact with one another through an intermolecular three-helix bundle (Figure S4) (Bochkareva et al., 2002). Notably, in the RMI1C-RMI2 crystal structure, neither RMI1C nor RMI2 would interfere with the association of a third subunit if it binds to the complex in the same manner as in RPA (Figure S4). Hence, it is possible that the current complex still misses another OB-fold containing protein, which together with RMI1 and RMI2 could form an RPA-like ternary complex. Further studies are required to test this hypothesis.

Notwithstanding the high degree of overall structural conservation, there are substantial differences between the RMI1C-RMI2 and the RPA70C-RPA32N complexes. First, the relative positions between the two components are different in the two complexes. When both complex structures are overlaid based on the OB-folds of RMI1C and RPA70C, the β-barrel of RMI2 exhibits a ~6 Å shift toward RMI1C relative to the position of the β-barrel in RPA32N (Figure 5A). Second, RPA70C contains a zinc ribbon motif embedded in the OB-fold between strands β1 and β2, which might play a role in ssDNA binding (Figure 5A) (Lao et al., 1999; Park et al., 1999; Walther et al., 1999). In contrast, strands β1 and β2 in RMI1C are connected by a short seven-residue loop (residues 522-528). This structural difference is consistent with the finding that, unlike the RPA complex, the RMI1-RMI2 complex failed to display ssDNA-binding activity (Xu et al., 2008a).

Mutational and functional analyses of the RMI1C-RMI2 interaction

To corroborate our structural analysis, we examine whether missense mutation of the interface residues of RMI2 observed in the crystal structure could weaken or disrupt the RMI1-RMI2 interaction. We first focused on the hydrophobic interface between the two C-terminal helices in the RMI1C-RMI2 complex. In particular, located at the center of this interface, the side chain of Met134 of RMI2 is nested in a pocket formed by a group of hydrophobic residues of RMI1C (Figure 4C). IP experiments revealed that while wild-type RMI2 showed the expected interaction with RMI1, substitution of RMI2 Met134 with a positively charged and bulkier arginine residue completely abolished the interaction with

RMI1 in cells (Figure 6A). By contrast, mutations I130R and L137R of RMI2, also designed to eliminate the hydrophobic interface in the complex still maintained the RMI1 binding activity, indicating that these residues are not essential for binding (Figure 6A). Notably, although RMI2 does not directly interact with BLM or Topo IIIα, wild-type RMI2 or the I130R and L137R mutant proteins could efficiently co-precipitated endogenous BLM and Topo IIIα, conforming that RMI1 functions as an interaction hub in the complex (Figure 6A, lanes 2, 3, and 5). Next, to investigate the importance of the electrostatic interactions between RMI1 and RMI2, Asp141 of RMI2 was mutated to either an alanine or arginine residue and their effects on the RMI1-RMI2 interaction were assessed by IP. In the crystal structure, Asp141 mediates three electrostatic interactions with two RMI1 residues at the binding interface (Figure 4B). As shown in Figure 6A, both mutations completely abrogated the RMI1-RMI2 interaction in cells. Collectively, we conclude that both the hydrophobic and the electrostatic contacts observed in the crystal structure are crucial for the interaction between RMI1 and RMI2.

Although RMI1N itself is sufficient to stimulate dHJ dissolution activity of BLM and Topo IIIα *in vitro* (Fig. 3A), RMI2 is required for the *in vivo* stability of the BLM complex (Singh et al., 2008; Xu et al., 2008a). To address the *in vivo* consequence of the RMI1-RMI2 interaction, we first tested whether RMI2 mutants that were deficient in RMI1 binding could protect RMI1 and Topo IIIα from proteolysis in the absence of endogenous RMI2. As shown in Figure 6B, when endogenous RMI2 is compromised by siRNA treatment, a decrease in Topo IIIα and RMI1 is observed (compare lanes 1 and 2) (Singh et al., 2008). This decreased level of Topo IIIα and RMI1 was nearly completely rescued by stable expression of His_6-FLAG-tagged (HF) wild-type or the I130R mutant of RMI2 before the siRNA treatment (Figure 6B, lanes 3-6). In contrast, expression of the RMI1-binding deficient mutants of RMI2 (M134R and D141R) in RMI2-depleted cells did not prevent the degradation of Topo IIIα and RMI1 (Figure 6B, lanes 7-10). We previously reported that RMI2-depleted cells exhibited methyl methanesulfonate (MMS) sensitivity (Singh et al., 2008). Next, we examined whether expression of RMI1-binding deficient mutants of RMI2 in RMI2-depleted cells could rescue the MMS sensitivity. While wild-type RMI2 and the I130R mutant completely rescued the MMS sensitivity, substitution of endogenous RMI2 with the M134R or the D141R mutants showed hypersensitivity to MMS that was comparable with RMI2-depleted cells (Figure 6C). Collectively, these data suggests that the interaction between RMI1 and RMI2 is essential for the *in vivo* functions of RMI2. Although RMI1N itself is sufficient to stimulate dHJ dissolution activity of BLM and Topo IIIα *in vitro* (Fig. 3A), RMI2, which is recruited by RMI1C *in vivo*, is still required for the overall stability of the entire dissovasome complex (Fig. 6). Therefore, the RMI1-RMI2 complex is crucial for the dissovasome complex formation and its proper function.

Discussion

Both RMI1 and RMI2 play important roles in BLM-dependent genome maintenance. They were predicted to contain OB-folds (Singh et al., 2008; Xu et al., 2008a). However, unlike most OB-fold-containing proteins that associate with nucleic acids, RMI1 and RMI2 primarily mediate protein-protein interactions in the BLM complex. RMI1 interacts with all the other three subunits in the complex. Consistent with its biological function, the structure

of RMI1 is organized into three distinct regions: an N-terminal BLM- and Topo IIIα-binding domain (RMI1N), a random-coiled linker region, and a C-terminal RMI2 binding domain (RMI1C). Notably, it has been proposed that RMI1C binds RMI2 to form an RPA-like complex (Xu et al., 2008a). However, the relationship between RMI1-RMI2 and the RPA complex remains unclear due to the lack of structural information on RMI1-RMI2. In this study, we provide the first direct evidence for the existence of multiple OB-folds in RMI1 and RMI2 (Figure 1A). Our structural data reveals a striking structural similarity between RMI1C-RMI2 and the RPA70C-RPA32N subcomplex in RPA. In both cases, the hetero-oligomerization is required for the stability of the complex. However, despite these similarities, there are substantial differences between RMI-RMI2 and RPA. Unlike RPA70, RMI1 only contains two OB folds and lacks the middle two OB folds that are essential for efficient DNA binding. In addition, the RMI1-RMI2 complex does not have an equivalent subunit of RPA14 in RPA. These marked differences favor the possibility of convergent evolution as the explanation for the resemblance between RMI1-RMI2 and the RPA proteins. In other words, these proteins may not share a common ancestor, but may have evolved similar domains because of their functional requirement.

The OB-fold in RMI1N contains two unique motifs: an N-terminal three-helix bundle and a large insertion between strands β1 and β2. The insertion extends out from the OB-fold core to mediate the interactions with BLM and Topo IIIα and is critical for the robust dHJ dissolution activity of the BLM complex. Unlike the insertion motif, the three-helix bundle is required for the proper folding RMI1N. Structure database search reveals that the three-helix bundle in RMI1N is most similar to domain III in *Mycobacterium tuberculosis* MtRuvA (Prabu et al., 2006); the two three-helix bundles can be superimposed with an rmsd of 2.5 Å in the positions of 50 equivalent Cα atoms (Figure S5). In prokaryotes, Holliday junction (HJ) is processed by the RuvA-RuvB-RuvC complex (Ingleston et al., 2000; Nishino et al., 2000). MtRuvA contains three domains; domains I and II are responsible for HJ binding and domain III is a mobile element that is required for binding of MtRuvB and plays an important role in branch migration (Nishino et al., 1998; Rafferty et al., 1996). In eukaryotes, the BLM complex processes the dHJ dissolution via two key steps. First, BLM catalyzes the convergent branch migration of the two individual HJs to form the hemicatenane intermediate. Second, Topo IIIα mediates the decatenation of the hemicatenated intermediate. The structural resemblance of the three-helix-bundles in RMI1 and RuvA and the functional importance of the insertion motif in RMI1 prompt us to speculate that RMI1 might be actively involved in both steps. RMI1 might be a functional ortholog of RuvA in dHJ dissolution, and play a regulatory role in branch migration through association with BLM. Furthermore, via the insertion motif, RMI1 associates with Topo IIIα and stimulates its enzymatic activity to decatenate the hemicatenated intermediate. Detailed structural and functional analyses of the entire BLM complex are needed to test these possibilities and reveal the functional significance of RMI1 and RMI2 in regulating BLM-Topo IIIα-mediated dHJ dissolution.

Experimental Procedures

Protein expression and purification

The RMI1C-RMI2 complex—Human RMI1C (residues 475-625) was cloned into a GST fusion protein expression vector, pGEX6p-1 (GE Healthcare). RMI2 (residues 6–147) was cloned into a modified His_6-Sumo-pET28b vector (Mossessova and Lima, 2000; Wang et al., 2007). The two plasmids were cotransformed into *E. coli* Rosetta DE3 strain. Positive colonies bearing both plasmids were selected under Amp/Kana double selection. After induction for 16 hours with 0.1 mM IPTG at 25 °C, the cells were harvested by centrifugation and the pellets were resuspended in lysis buffer (50 mM Tris-HCl pH 8.0, 50 mM NaH_2PO_4, 400 mM NaCl, 10% glycerol, 1mM PMSF, 0.1 mg/ml lysozyme, 2mM 2-mercaptoethanol, and home-made protease inhibitor cocktail). The cells were then lysed by sonication and the cell debris was removed by ultracentrifugation. The supernatant was mixed with glutathione sepharose beads (GE Healthcare) and rocked for 6 hours at 4 °C before elution with 15 mM reduced glutathione. The protease 3C was added to remove the GST-tag. The complex was then mixed with Ni-NTA agarose beads (Qiagen) and rocked for 8 hours at 4 °C before elution with 250 mM imidazole. The ULP1 protease was added to remove the His_6-Sumo tag. Finally the RMI1C-RMI2 complex was further purified by gel-filtration chromatography on Hiload Superdex 75. The purified RMI1C-RMI2 complex protein was concentrated to 25 mg/ml and stored at −80 °C. The Se-Met-labeled RMI1C-RMI2 complex was expressed in M9 minimal media containing Se-Met and purified following the same procedure as described above.

RMI1N—Human RMI1N (rediues 2–213) and the deletion mutant RMI1NΔLoop (residues 97–132 replaced by an SGGS linker) were cloned into the His_6-Sumo-pET28b vector. Protein expression was carried out in *E. coli* strain BL21(DE3) for 16 hours after induction with 0.1 mM IPTG at 25 °C. The proteins were purified following the same procedures as described above except for only one affinity chromatography step (Ni-NTA agarose) was used. The Se-Met-labeled RMI1N was expressed in M9 minimal media containing Se-Met.

Crystallization, data collection and structure determination

RMI1N—Crystals were grown by hanging drop vapor diffusion method at 4 °C. The well solution contained 100 mM Tris-HCl pH 8.5, 18% PEG 3350, 300 mM NaSCN, 10 mM $NiCl_2$ and 10 mM DTT. Crystals were gradually transferred to a harvesting solution (100 mM Tris-HCl pH 8.5, 25% PEG 3350, 25% glycerol, 300 mM NaSCN, 10 mM $NiCl_2$ and 10 mM DTT) before being flash-frozen in liquid nitrogen. Se-Met-SAD dataset at 2.0 Å resolution was collected at beamline 21ID-D at APS and processed using HKL2000 (Otwinowski, 1997). Crystals belong to space group $P3_121$ with one complex per asymmetric unit. Five selenium sites were located and refined, and SAD phases calculated using SHARP (La Fortelle, 1997). A model was automatically built into the modified experimental electron density using ARP/WARP (Lamzin, 2001); the model was then further refined using simulated-annealing and positional refinement in CNS (Brunger et al., 1998) with manual rebuilding using program O (Jones et al., 1991).

The RMI1C-RMI2 complex—Crystals were grown by hanging drop vapor diffusion method at 4 °C. The well solution contained 18% PEG 3350, 300 mM NaSCN, and 10 mM DTT. Crystals were gradually transferred to a harvesting solution (25% PEG 3350, 25% glycerol, 300 mM NaSCN, and 10 mM DTT) before being flash-frozen in liquid nitrogen. Se-Met-SAD dataset at a resolution of 2.0 Å was collected at beamline 21ID-D at APS and processed using HKL2000 (Otwinowski, 1997). Crystals belong to space group $P2_12_12_1$ with one complex per asymmetric unit. Eleven selenium sites were located and refined, and SAD phases calculated using SHARP (La Fortelle, 1997). Model building and refinement were carried out following the same procedure as those for RMI1C described above.

dHJ Dissolution assay

The dHJ dissolution reaction is carried out in the presence of BLM (10 nM), Topo IIIα (125 nM), and RMI1 (MBP-RMI1, RMI1N, RMI1NΔLoop) (5, 10, 15, and 20 nM) were incubated for 10 min on ice in 12 μl reaction buffer (50 mM Tris-HCl, pH 7.8, 1 mM DTT, 0.8 mM $MgCl_2$, 200 μg/ml BSA, 2 mM ATP, 80 mM of KCl, and an ATP regenerating system consisting of 10 mM creatine phosphate and 50 μg/ml creatine kinase) followed by the addition of the dHJ substrate (1 nM). After a 5-min incubation at 37 °C, 2 μl of 1% SDS and 1 μl of proteinase K (10 μg/μl stock) were added to the reaction mixtures, followed by a 10 min incubation at 37 °C. The deproteinized reactions were mixed with an equal volume of sample loading buffer (20 mM Tris-HCl, pH 7.5, 50% glycerol, and 0.08% Orange G) containing 50% urea, incubated at 95 °C for 3 min, and then resolved in 8% denaturing gels.

Immunoprecipitation

Immunoprecipitation was performed using the protocol described previously (Yin et al., 2005). Polyclonal antibodies against BLM, Topo IIIa, RMI1, and RMI2 were described previously (Meetei et al., 2003; Singh et al., 2008; Wu et al., 2000; Xu et al., 2008a; Yin et al., 2005). Cells were lysed in NP buffer (25 mM Tris-HCl pH 7.5, 150 mM NaCl, 0.5% NP-40, 5% glycerol, 1 mM DTT, protease inhibitor cocktail, 1mM PMSF). Coimmunoprecipitation was performed using the anti-Flag M2-agarose (Sigma).

Protein knockdown by siRNA treatment

All siRNA oligos were purchased from Dharmacon. For the knockdown of RMI2, we designed an siRNA in the 3′UTR (3′UTR1C: 5′-UGUUGGAACUGUCGUUAAAUU-3′), a nonspecific control siRNA (catalog no. D-001210-01) was used in all experiments. Cells were transfected with siRNA using lipofectamine2000 for 5 h in reduced serum OptiMEM medium, as recommended by the manufacturer (Invitrogen). After 5 h, OptiMEM was removed and replaced by complete DMEM medium. Cells were harvested 4 days post-transfection and analyzed by immunoblotting.

Construction of $(His)_6$-FLAG-tagged (HF) RMI2 mutants plasmids and generation of retroviruses

$(His)_6$-FLAG-tagged (HF) RMI2 were generated by PCR mediated site directed mutagenesis and cloned at the BamH1 and Xho1 sites of the PMIEG3 vector to generate pMIEGs-HF-RMI2. The pMIEG3 retroviral vector and the generation of retroviruses were as described

earlier (Singh et al., 2008). Briefly, amphotropic retroviruses were created and used to infect the target cells. To prepare transient virus stocks, 1.5×10^6 293T cells were plated in 10-cm dishes. The next day, cells were cotransfected using lipofectamine2000 with the retroviral expression vectors as described above, together with the appropriate helper plasmid (gag-pol and RD114). The medium was changed 5 h post-transfection, and retrovirus-containing medium was harvested in 12-h increments at 24 h post-transfection.

Generation of stable cell lines

Cells were seeded in six-well plates at the density of 5×10^4 cells per well in 3 mL of complete medium. The next day, cells were transduced in the presence of 8 ng/mL polybrene (Sigma Aldrich). The plates were then spun at 1000 g for 1 h, transferred to a humidified incubator (5% CO_2), and cultured for 17 hat 37°C. Cells were washed twice to remove polybrene and resuspended in complete DMEM medium (GIBCO-BRL). After culture for 48–72 h, the EGFP-positive cells were sorted using a Becton Dickinson FACS antage SE instrument (Becton Dickinson Immunocytometry Systems).

MMS sensitivity assay

Methyl methanesulfonate (MMS) was purchased from Sigma. A stock solution was diluted to 2000 μM with DMSO. HeLa cells stably expressing wild-type or different mutants of RMI2 were transfected with siRNA targeting RMI2, or control oligos, as described above. At 3 days post-transfection, 200 cells were seeded per 10-cm dish containing the indicated concentration of MMS in DMEM medium. After 10 d cells were fixed, stained, and visible colonise were counted.

Supplementary Material

Refer to Web version on PubMed Central for supplementary material.

Acknowledgments

We thank Y. Chen and J. Sun for help at various stages of the project. M.L. is a Howard Hughes Medical Institute Early Career Scientist. This work was supported by NIH grants (GM 083015-01 to M.L., HL084082 to A.R.M., and ES015632 and ES07061 to P.S.), an American Cancer Society Research Scholar Award (to M.L.), and the Intramural Research Program of the National Institute on Aging (AG000688-07 to W.W.). The General Medicine and Cancer Institutes Collaborative Access Team has been funded in whole or in part with federal funds from the National Cancer Institute (grant Y1-CO-1020) and the National Institute of General Medical Science (grant Y1-GM-1104). Use of the Advanced Photon Source was supported by the U.S. Department of Energy, Office of Science, Office of Basic Energy Sciences, under contract no. DE-AC02-06CH11357.

References

Bachrati CZ, Hickson ID. RecQ helicases: guardian angels of the DNA replication fork. Chromosoma. 2008; 117:219–233. [PubMed: 18188578]

Beamish H, Kedar P, Kaneko H, Chen P, Fukao T, Peng C, Beresten S, Gueven N, Purdie D, Lees-Miller S, et al. Functional link between BLM defective in Bloom's syndrome and the ataxia-telangiectasia-mutated protein, ATM. J Biol Chem. 2002; 277:30515–30523. [PubMed: 12034743]

Bennett RJ, Noirot-Gros MF, Wang JC. Interaction between yeast sgs1 helicase and DNA topoisomerase III. J Biol Chem. 2000; 275:26898–26905. [PubMed: 10862619]

Bochkarev A, Bochkareva E. From RPA to BRCA2: lessons from single-stranded DNA binding by the OB-fold. Curr Opin Struct Biol. 2004; 14:36–42. [PubMed: 15102447]

Bochkarev A, Bochkareva E, Frappier L, Edwards AM. The crystal structure of the complex of replication protein A subunits RPA32 and RPA14 reveals a mechanism for single-stranded DNA binding. EMBO J. 1999; 18:4498–4504. [PubMed: 10449415]

Bochkarev A, Pfuetzner RA, Edwards AM, Frappier L. Structure of the single-stranded-DNA-binding domain of replication protein A bound to DNA. Nature. 1997; 385:176–181. [PubMed: 8990123]

Bochkareva E, Korolev S, Lees-Miller SP, Bochkarev A. Structure of the RPA trimerization core and its role in the multistep DNA-binding mechanism of RPA. EMBO J. 2002; 21:1855–1863. [PubMed: 11927569]

Briggs GS, Mahdi AA, Wen Q, Lloyd RG. DNA binding by the substrate specificity (wedge) domain of RecG helicase suggests a role in processivity. J Biol Chem. 2005; 280:13921–13927. [PubMed: 15695524]

Brunger AT, Adams PD, Clore GM, DeLano WL, Gros P, Grosse-Kunstleve RW, Jiang JS, Kuszewski J, Nilges M, Pannu NS, et al. Crystallography & NMR system: A new software suite for macromolecular structure determination. Acta Crystallogr D Biol Crystallogr. 1998; 54:905–921. [PubMed: 9757107]

Bussen W, Raynard S, Busygina V, Singh AK, Sung P. Holliday junction processing activity of the BLM-Topo IIIalpha-BLAP75 complex. J Biol Chem. 2007; 282:31484–31492. [PubMed: 17728255]

Chang M, Bellaoui M, Zhang C, Desai R, Morozov P, Delgado-Cruzata L, Rothstein R, Freyer GA, Boone C, Brown GW. RMI1/NCE4, a suppressor of genome instability, encodes a member of the RecQ helicase/Topo III complex. EMBO J. 2005; 24:2024–2033. [PubMed: 15889139]

Chen CF, Brill SJ. Binding and activation of DNA topoisomerase III by the Rmi1 subunit. J Biol Chem. 2007; 282:28971–28979. [PubMed: 17693398]

Davies SL, North PS, Dart A, Lakin ND, Hickson ID. Phosphorylation of the Bloom's syndrome helicase and its role in recovery from S-phase arrest. Mol Cell Biol. 2004; 24:1279–1291. [PubMed: 14729972]

Ellis NA, Groden J, Ye TZ, Straughen J, Lennon DJ, Ciocci S, Proytcheva M, German J. The Bloom's syndrome gene product is homologous to RecQ helicases. Cell. 1995; 83:655–666. [PubMed: 7585968]

Gangloff S, McDonald JP, Bendixen C, Arthur L, Rothstein R. The yeast type I topoisomerase Top3 interacts with Sgs1, a DNA helicase homolog: a potential eukaryotic reverse gyrase. Mol Cell Biol. 1994; 14:8391–8398. [PubMed: 7969174]

Holm L, Sander C. Database algorithm for generating protein backbone and side-chain co-ordinates from a C alpha trace application to model building and detection of co-ordinate errors. J Mol Biol. 1991; 218:183–194. [PubMed: 2002501]

Horvath MP, Schweiker VL, Bevilacqua JM, Ruggles JA, Schultz SC. Crystal structure of the Oxytricha nova telomere end binding protein complexed with single strand DNA. Cell. 1998; 95:963–974. [PubMed: 9875850]

Ingleston SM, Sharples GJ, Lloyd RG. The acidic pin of RuvA modulates Holliday junction binding and processing by the RuvABC resolvasome. EMBO J. 2000; 19:6266–6274. [PubMed: 11080172]

Jacobs DM, Lipton AS, Isern NG, Daughdrill GW, Lowry DF, Gomes X, Wold MS. Human replication protein A: global fold of the N-terminal RPA-70 domain reveals a basic cleft and flexible C-terminal linker. J Biomol NMR. 1999; 14:321–331. [PubMed: 10526407]

Jones TA, Zou JY, Cowan SW, Kjeldgaard M. Improved methods for building protein models in electron density maps and the location of errors in these models. Acta Crystallogr A. 1991; 47(Pt 2):110–119. [PubMed: 2025413]

Kerr ID, Wadsworth RI, Cubeddu L, Blankenfeldt W, Naismith JH, White MF. Insights into ssDNA recognition by the OB fold from a structural and thermodynamic study of Sulfolobus SSB protein. EMBO J. 2003; 22:2561–2570. [PubMed: 12773373]

La Fortelle, Ed, Bricogne, G. In Method in Enzymology. Academic Press; 1997. Maximum-likehood Heavy-Atom Parameter Refinement for Multiple Isomorphous Replacement and Multiwavelength Anomalous Diffraction Methods; p. 472-494.

Lamzin, VS., Perrakis, A., Wilson, KS. The ARP/WARP suite for automated construction and refinement for protein models. In: Rossmann, MG., Arnold, E., editors. Int Tables for Crystallography Vol F: Crystallography of biological macromolecules. Dordrecht, Kluwer Academic Publishers; The Netherlands: 2001. p. 720-722.

Lao Y, Lee CG, Wold MS. Replication protein A interactions with DNA. 2. Characterization of double-stranded DNA-binding/helix-destabilization activities and the role of the zinc-finger domain in DNA interactions. Biochemistry. 1999; 38:3974–3984. [PubMed: 10194309]

Lei M, Podell ER, Baumann P, Cech TR. DNA self-recognition in the structure of Pot1 bound to telomeric single-stranded DNA. Nature. 2003; 426:198–203. [PubMed: 14614509]

Lei M, Podell ER, Cech TR. Structure of human POT1 bound to telomeric single-stranded DNA provides a model for chromosome end-protection. Nat Struct Mol Biol. 2004; 11:1223–1229. [PubMed: 15558049]

Meetei AR, Sechi S, Wallisch M, Yang D, Young MK, Joenje H, Hoatlin ME, Wang W. A multiprotein nuclear complex connects Fanconi anemia and Bloom syndrome. Mol Cell Biol. 2003; 23:3417–3426. [PubMed: 12724401]

Mitton-Fry RM, Anderson EM, Theobald DL, Glustrom LW, Wuttke DS. Structural basis for telomeric single-stranded DNA recognition by yeast Cdc13. J Mol Biol. 2004; 338:241–255. [PubMed: 15066429]

Mossessova E, Lima CD. Ulp1-SUMO crystal structure and genetic analysis reveal conserved interactions and a regulatory element essential for cell growth in yeast. Mol Cell. 2000; 5:865–876. [PubMed: 10882122]

Mullen JR, Nallaseth FS, Lan YQ, Slagle CE, Brill SJ. Yeast Rmi1/Nce4 controls genome stability as a subunit of the Sgs1-Top3 complex. Mol Cell Biol. 2005; 25:4476–4487. [PubMed: 15899853]

Nishino T, Ariyoshi M, Iwasaki H, Shinagawa H, Morikawa K. Functional analyses of the domain structure in the Holliday junction binding protein RuvA. Structure. 1998; 6:11–21. [PubMed: 9493263]

Nishino T, Iwasaki H, Kataoka M, Ariyoshi M, Fujita T, Shinagawa H, Morikawa K. Modulation of RuvB function by the mobile domain III of the Holliday junction recognition protein RuvA. J Mol Biol. 2000; 298:407–416. [PubMed: 10772859]

Otwinowski, Z., Minor, W. Processing of X-ray Diffraction Data Collected in Oscillation Mode In Method in Enzymology. Academic Press; 1997. p. 307-326.

Park JS, Wang M, Park SJ, Lee SH. Zinc finger of replication protein A, a non-DNA binding element, regulates its DNA binding activity through redox. J Biol Chem. 1999; 274:29075–29080. [PubMed: 10506160]

Plank JL, Wu J, Hsieh TS. Topoisomerase IIIalpha and Bloom's helicase can resolve a mobile double Holliday junction substrate through convergent branch migration. Proc Natl Acad Sci U S A. 2006; 103:11118–11123. [PubMed: 16849422]

Prabu JR, Thamotharan S, Khanduja JS, Alipio EZ, Kim CY, Waldo GS, Terwilliger TC, Segelke B, Lekin T, Toppani D, et al. Structure of Mycobacterium tuberculosis RuvA, a protein involved in recombination. Acta Crystallogr Sect F Struct Biol Cryst Commun. 2006; 62:731–734.

Rafferty JB, Sedelnikova SE, Hargreaves D, Artymiuk PJ, Baker PJ, Sharples GJ, Mahdi AA, Lloyd RG, Rice DW. Crystal structure of DNA recombination protein RuvA and a model for its binding to the Holliday junction. Science. 1996; 274:415–421. [PubMed: 8832889]

Ralf C, Hickson ID, Wu L. The Bloom's syndrome helicase can promote the regression of a model replication fork. J Biol Chem. 2006; 281:22839–22846. [PubMed: 16766518]

Raynard S, Bussen W, Sung P. A double Holliday junction dissolvasome comprising BLM, topoisomerase IIIalpha, and BLAP75. J Biol Chem. 2006; 281:13861–13864. [PubMed: 16595695]

Raynard S, Zhao W, Bussen W, Lu L, Ding YY, Busygina V, Meetei AR, Sung P. Functional role of BLAP75 in BLM-topoisomerase IIIalpha-dependent holliday junction processing. J Biol Chem. 2008; 283:15701–15708. [PubMed: 18390547]

Rost B, Yachdav G, Liu J. The PredictProtein server. Nucleic Acids Res. 2004; 32:W321–326. [PubMed: 15215403]

Singh TR, Ali AM, Busygina V, Raynard S, Fan Q, Du CH, Andreassen PR, Sung P, Meetei AR. BLAP18/RMI2, a novel OB-fold-containing protein, is an essential component of the Bloom helicase-double Holliday junction dissolvasome. Genes Dev. 2008; 22:2856–2868. [PubMed: 18923083]

Sun J, Yu EY, Yang Y, Confer LA, Sun SH, Wan K, Lue NF, Lei M. Stn1-Ten1 is an Rpa2-Rpa3-like complex at telomeres. Genes Dev. 2009; 23:2900–2914. [PubMed: 20008938]

Walther AP, Gomes XV, Lao Y, Lee CG, Wold MS. Replication protein A interactions with DNA. 1. Functions of the DNA-binding and zinc-finger domains of the 70-kDa subunit. Biochemistry. 1999; 38:3963–3973. [PubMed: 10194308]

Wang F, Podell ER, Zaug AJ, Yang Y, Baciu P, Cech TR, Lei M. The POT1-TPP1 telomere complex is a telomerase processivity factor. Nature. 2007; 445:506–510. [PubMed: 17237768]

Wu L, Davies SL, North PS, Goulaouic H, Riou JF, Turley H, Gatter KC, Hickson ID. The Bloom's syndrome gene product interacts with topoisomerase III. J Biol Chem. 2000; 275:9636–9644. [PubMed: 10734115]

Wu L, Hickson ID. The Bloom's syndrome helicase suppresses crossing over during homologous recombination. Nature. 2003; 426:870–874. [PubMed: 14685245]

Xu D, Guo R, Sobeck A, Bachrati CZ, Yang J, Enomoto T, Brown GW, Hoatlin ME, Hickson ID, Wang W. RMI, a new OB-fold complex essential for Bloom syndrome protein to maintain genome stability. Genes Dev. 2008a; 22:2843–2855. [PubMed: 18923082]

Xu X, Vaithiyalingam S, Glick GG, Mordes DA, Chazin WJ, Cortez D. The basic cleft of RPA70N binds multiple checkpoint proteins, including RAD9, to regulate ATR signaling. Mol Cell Biol. 2008b; 28:7345–7353. [PubMed: 18936170]

Yin J, Sobeck A, Xu C, Meetei AR, Hoatlin M, Li L, Wang W. BLAP75, an essential component of Bloom's syndrome protein complexes that maintain genome integrity. EMBO J. 2005; 24:1465–1476. [PubMed: 15775963]

Zeng Z, Wang W, Yang Y, Chen Y, Yang X, Diehl JA, Liu X, Lei M. Structural basis of selective ubiquitination of TRF1 by SCFFbx4. Dev Cell. 18:214–225.

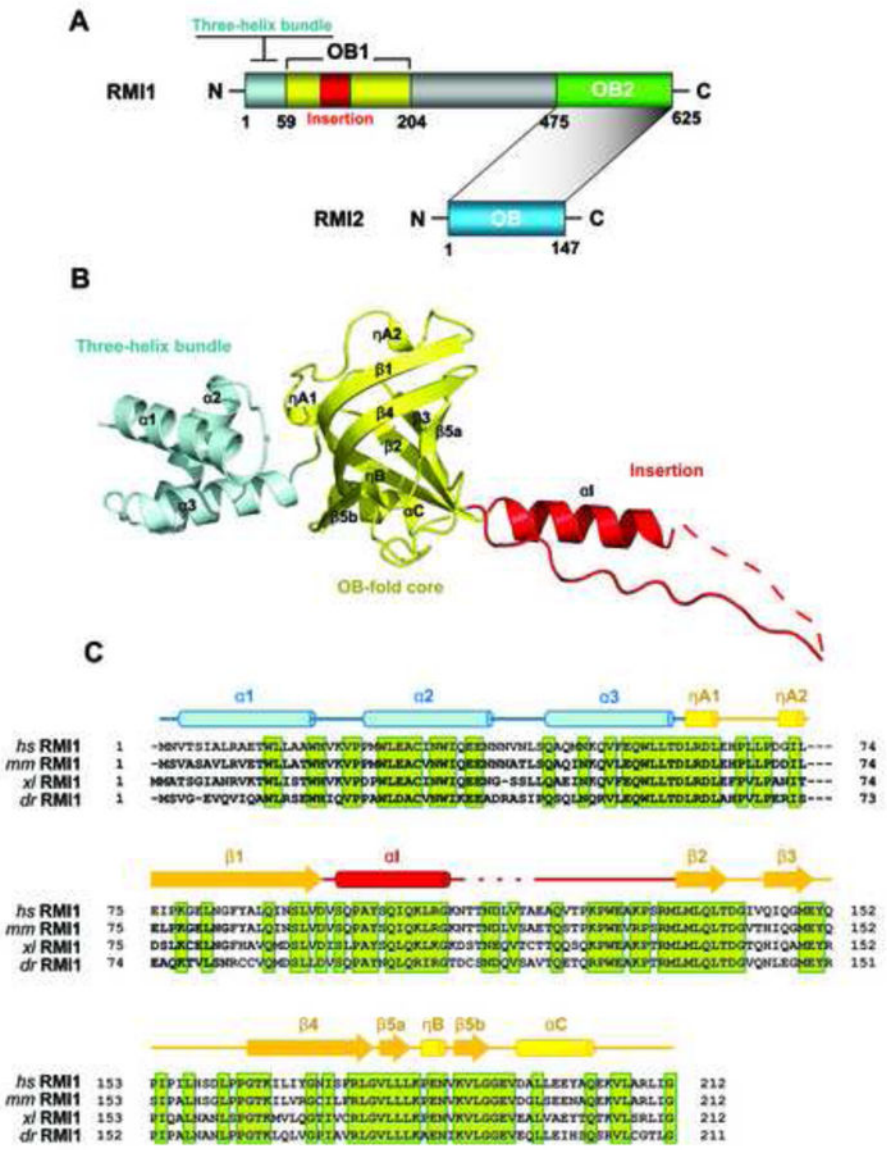

Figure 1.

Crystal structure of the N-terminal domain of human RMI1. **(A)** Domain organization of RMI1 and RMI2. In RMI1, the N-terminal three-helix bundle is colored in palecyan, the N-terminal OB-fold (OB1) in yellow, the insertion within OB1 in red, the middle linker region in grey, and the C-terminal OB-fold (OB2) in green. RMI2 is colored in cyan. The shaded area between RMI1 and RMI2 indicates that the RMI1-RMI2 interaction is mediated by the two OB-folds of both proteins. **(B)** Ribbon diagram of RMI1N. The three-helix buddle is colored in palecyan, OB-fold core in yellow, and the insertion in red. The dashed line indicates the unstructured region. **(C)** Amino acid sequence alignment of the N-terminal regions of the four representative vertebrate RMI1 family members (human, mouse, *Xenopus laevis, Danio rerio*). Secondary structure assignments based on the RMI1N crystal structure are shown as colored cylinders (α helices, 3_{10}(η)-helices) and arrows (β strands) above the sequences. Conserved residues are highlighted in green.

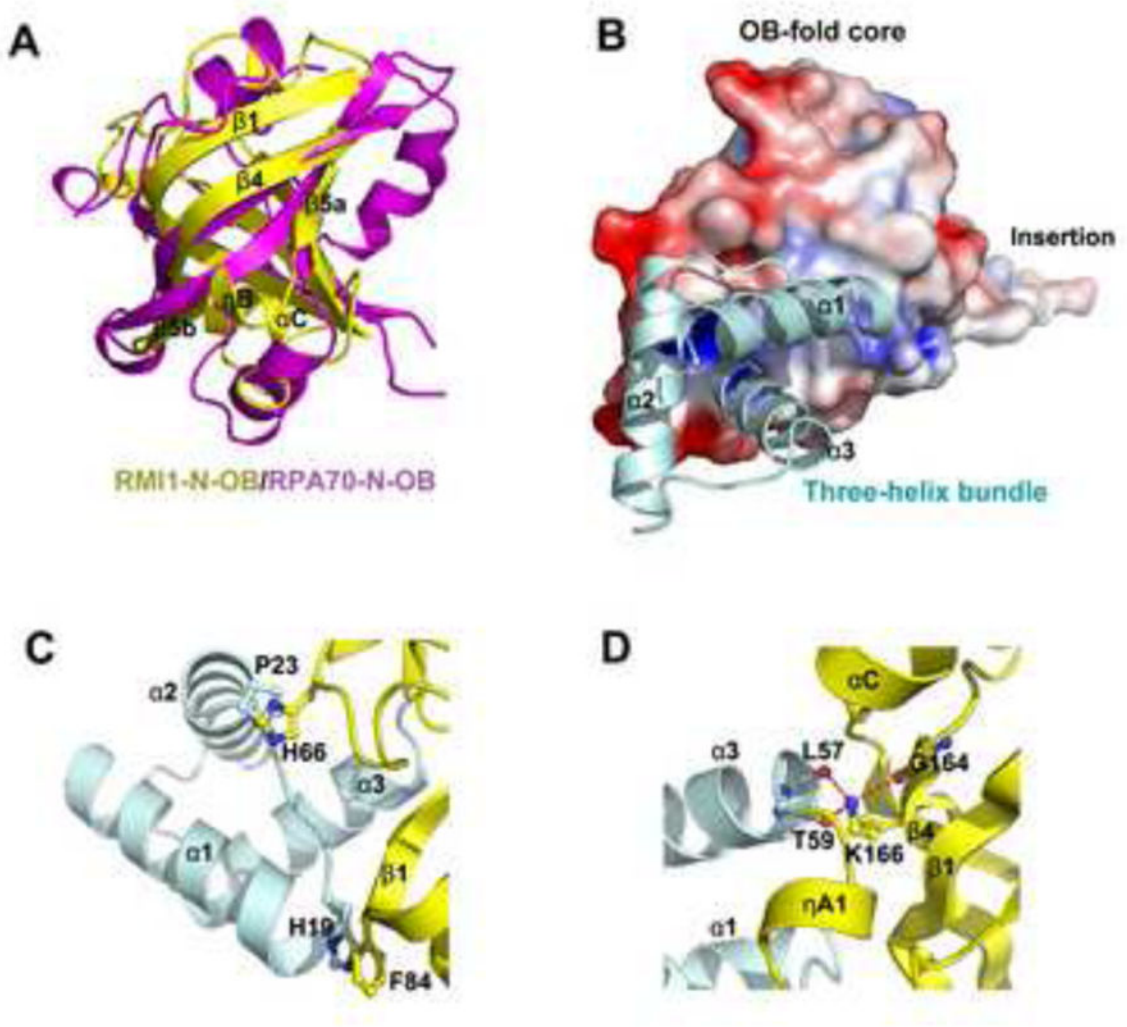

Figure 2.

Structural analysis of RMI1N. **(A)** Overlay of the OB-folds of RMI1N and RPA70N. RMI1N is colored in yellow and RPA70N in magenta. **(B)** The N-terminal three-helix bundle packs one a hydrophobic surface of the OB-fold core. The three-helix bundle is in ribbon representation and colored in palecyan. The OB-fold is in surface representation and colored according to its electrostatic potential (positive potential, blue; negative potential, red). **(C)** Two stacking interactions help stabilize the relative position between the three-helix bundle and the OB-fold core. The three-helix-bundle and the OB-fold core are in ribbon representation and colored in palecyan and yellow, respectively. The residues important for the interactions are shown as stick models. **(D)** Lys166 makes three hydrogen-bonding interactions (dashed magenta lines) with Leu57, Thr59, and Gly164. The three-helix-bundle motif and the OB-fold core are in ribbon representation and colored in palecyan and yellow, respectively. The interacting residues are shown as stick models.

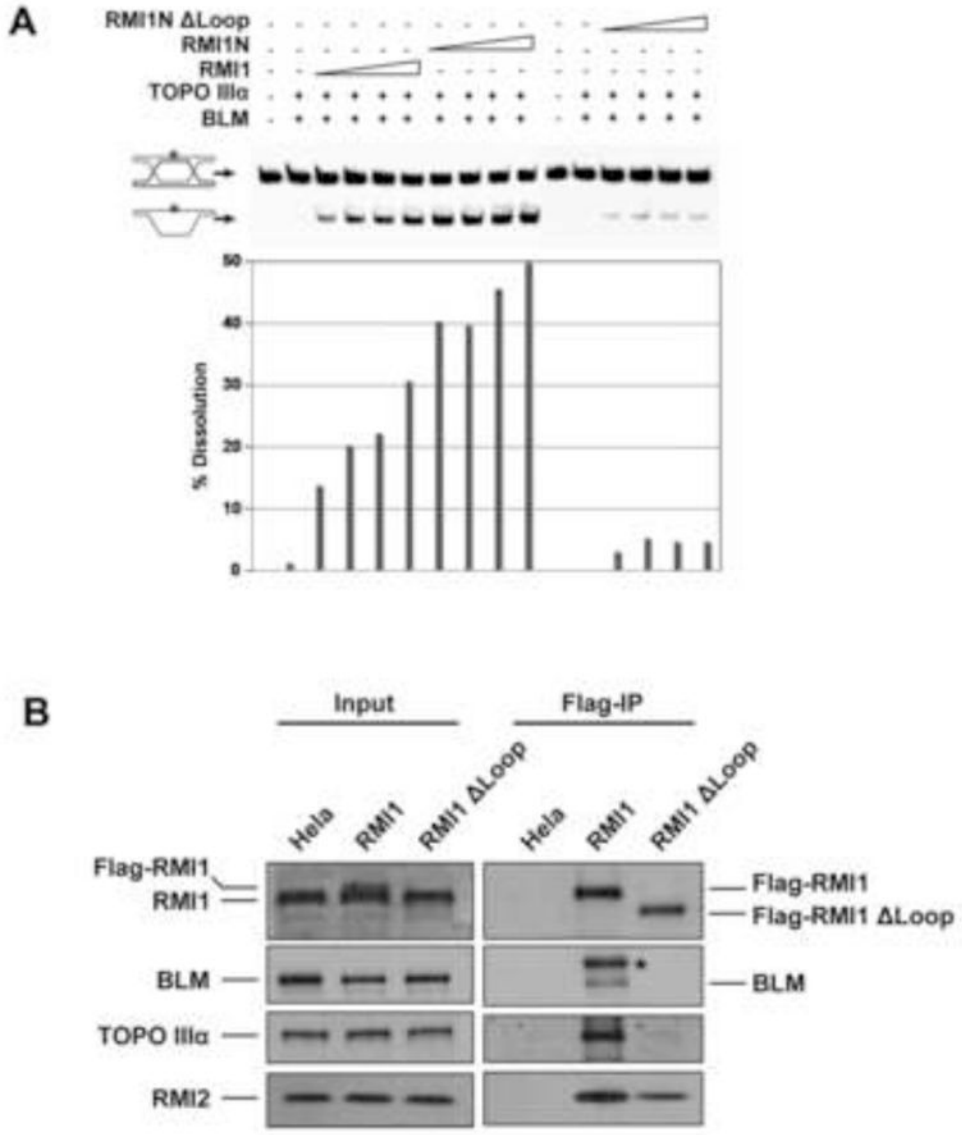

Figure 3.

The insertion motif in RMI1N is essential for enhancing the BLM-topo IIIα-mediated dHJ dissolution and for the *in vivo* association with BLM-Topo IIIα. **(A)** Increasing amount (5, 10, 15, and 20 nM) of RMI1, RMI1N and RMI1NΔLoop together with BLM-Topo IIIα were incubated with radiolabeled dHJ substrates (upper band). The reaction mixtures were resolved in polyacrylamide gels followed by Phosphorimaging analysis. Positions of the dHJ and product are marked. The histogram shows quantification of the levels of dissolution. **(B)** Immunoblotting shows that RMI1NΔLoop lost the binding activity with BLM-TOPOIIIα. Full-length Flag-RMI1 was co-immunoprecipitated with endogenous BLM, Topo IIIα, and RMI2. The asterisk indicates a non-specific band.

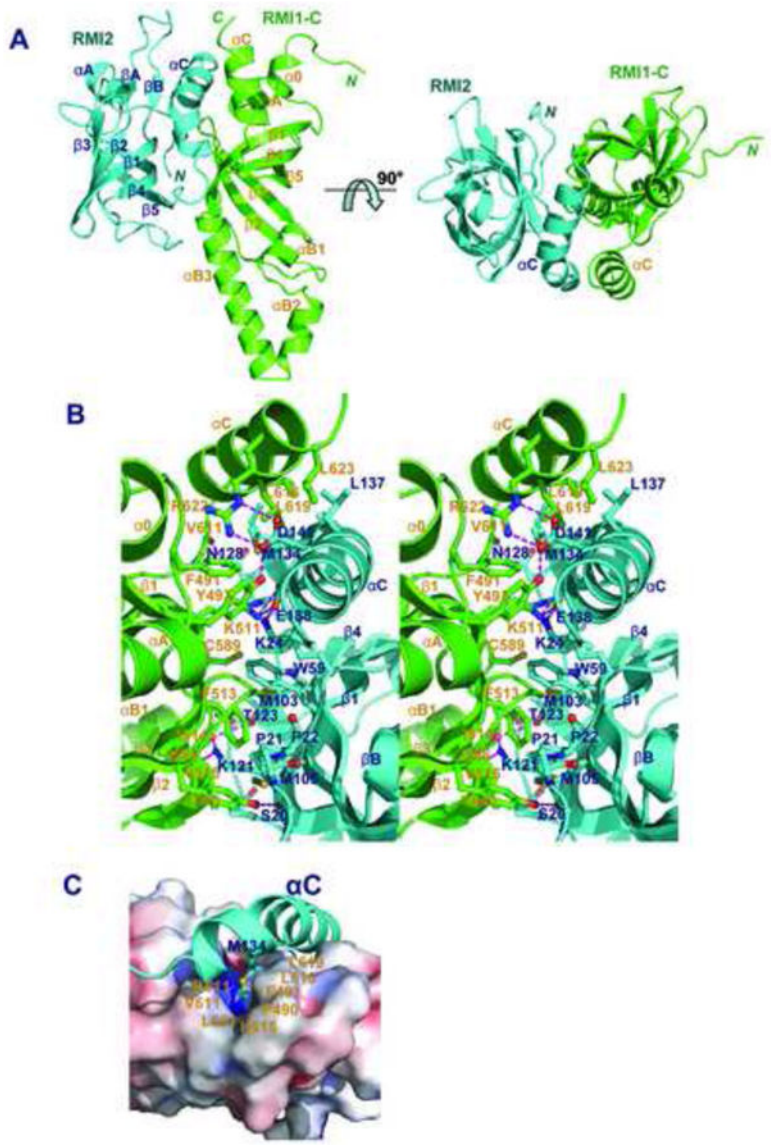

Figure 4.

Crystal structure of the RMI1C-RMI2 complex. **(A)** Ribbon diagram of two orthogonal views of the RMI1C-RMI2 complex. RMI1C and RMI2 are colored in green and cyan, respectively. The secondary structure elements are labeled. The RMI2C-RMI2 complex at right is rotated by 90° about a horizontal axis relative to the complex at left. **(B)** Stereo view of the interface between RMI1C and RMI2. RMI1C and RMI2 are colored as in (A). Side chains of residues important for the interaction are shown as stick models. The intermolecular hydrogen bonds are shown as dashed magenta lines. **(C)** The bended αC helix of RMI2 leans towards an extended groove formed by helix αC and one side of the OB-fold from RMI1C. RMI1C is in surface representation and colored according to its electrostatic potential. RMI2 is in ribbon representation and colored in cyan.

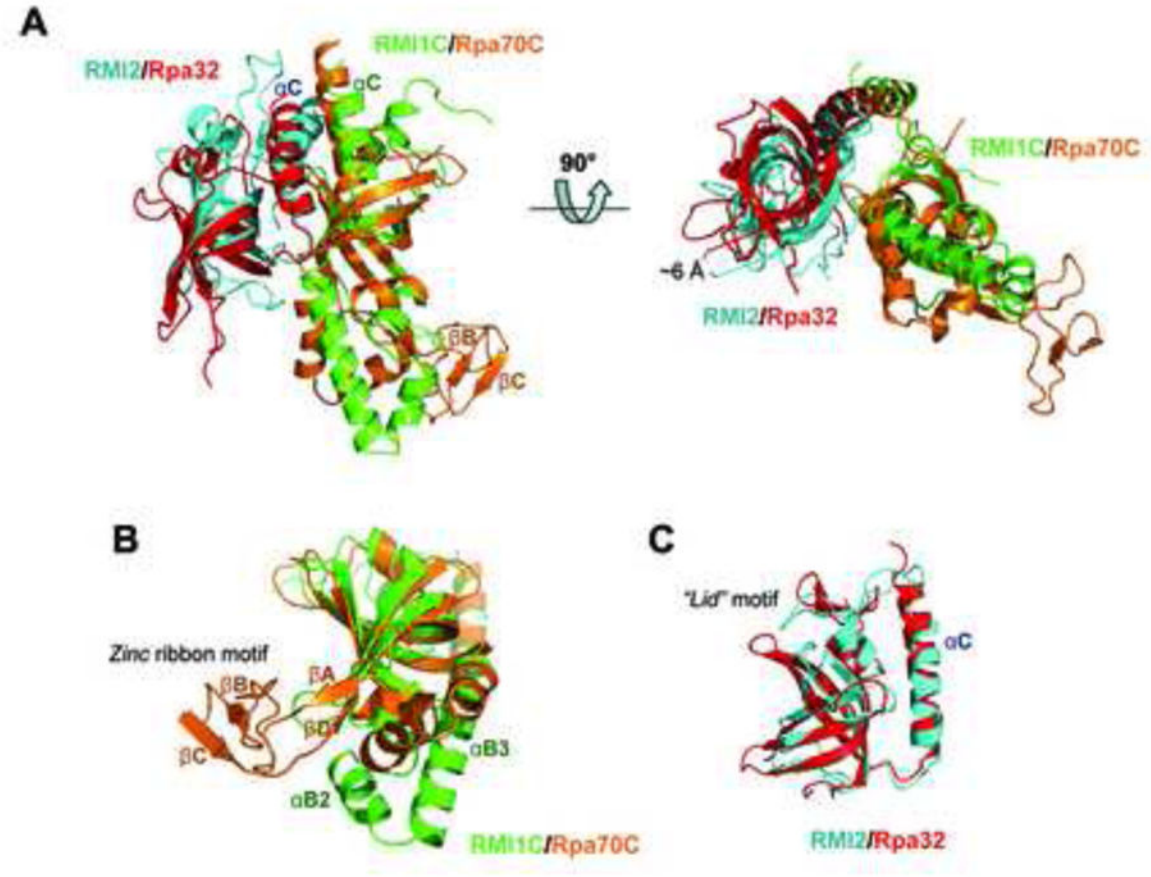

Figure 5.

The RMI1C-RMI2 complex is structurally similar to RPA70C-RPA32. **(A)** Superposition of the RMI1C-RMI2 complex on the crystal structure of the human RPA70C-RPA32N complex. RMI1C and RMI2 are colored in green and cyan, and RPA70C and RPA32N in orange and red. The superposition is based on the structures of RMI1C and RPA70C. RMI2 and RPA32N are not aligned well and RMI2 exhibits a ~ 6Å shift to RMI1C relative to the position of RPA32N. **(B)** Overlay of RMI1C and RPA70C based on the OB-fold β-barrels of the proteins. RMI1C lacks the Zinc ribbon motif in RPA70C. **(C)** Superposition of RMI2 and RPA32N based on the OB-fold β-barrels of the proteins. The “Lid” motif is also well aligned in the two structures.

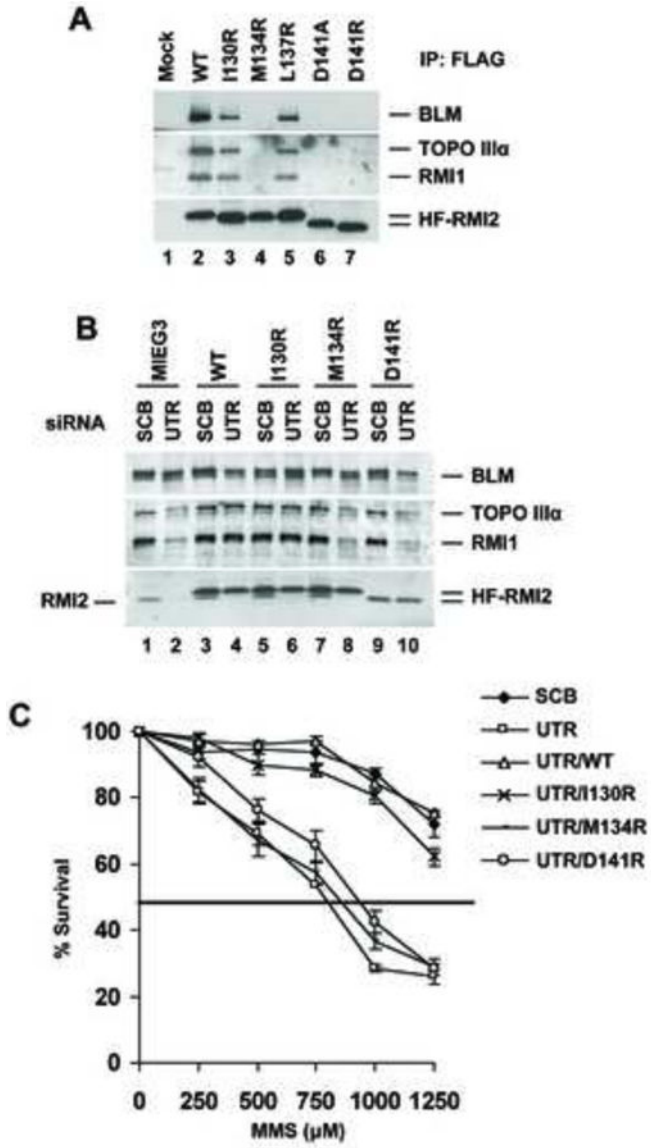

Figure 6.

Binding of RMI2 to RMI1 is essential for its *in vivo* functions. **(A)** Immunoprecipitation coupled with immunoblotting to assay for the binding of the various mutants of RMI2 to the BLM complex in HeLa cells**. (B)** Immunoblot showing the levels of BTB complex members in HeLa cells depleted of the endogenous RMI2. Note that when the endogenous RMI2 was specifically knocked down using siRNA targeting the 3′UTR of RMI2 cDNA, RMI2 mutants (M134R and D141R), which could not bind to BLM complex, were unable to protect Topo IIIα and RMI1 from degradation (lanes 8 and 10), while wild-type or the I130R mutant could rescue Topo IIIα and RMI1 from degradation (lanes 4 and 6). **(C)** Graph showing MMS survival curve of RMI2 knockdown HeLa cells, transduced with different variants of RMI2. HeLa cells stably expressing different variants of RMI2 were transfected with either scrambled siRNA (SCB) or siRNA targeting 3′UTR of RMI2 (UTR). At 3 days post-transfection, cells were subsequently treated with the indicated concentration

of MMS. Visible colonies from 200 cells were counted after 10 days. The data represent the percent survival, as compared with untreated cells. Each experiment was independently repeated three times and representative data are shown. Each experiment was performed in triplicate and mean values are shown with standard deviations.